Facile one-step preparation of 3D nanoporous Cu/Cu_6Sn_5 microparticles as anode material for lithium-ion batteries with superior lithium storage properties

Peng Xiang,[a] Wenbo Liu,[a,*] Xue Chen,[a] Shichao Zhang,[b] and Sanqiang Shi[c]

[a] School of Mechanical Engineering, Sichuan University, Chengdu 610065, China

[b] School of Materials Science and Engineering, Beihang University, Beijing 100191, China

[c] Department of Mechanical Engineering, The Hong Kong Polytechnic University, Hung Hom, Kowloon, Hong Kong 999077, China

Tel: +86-028-85405320; Fax: +86-028-85403408; E-mail: liuwenbo_8338@163.com.

Abstract

In this paper, three-dimensional nanoporous Cu/Cu_6Sn_5 microparticles (3D-NP Cu/Cu_6Sn_5 MPs) were prepared by one-step chemical dealloying of $Cu_{20}Sn_{80}$ (at. %) alloy slices in the mixed aqueous solution of HF and HNO_3, and filled into three-dimensional porous copper foam (3D-PCF) skeleton subsequently as anode (3D-PCF@Cu/Cu_6Sn_5) for lithium-ion batteries (LIBs). The results display that the ellipsoidal 3D-NP Cu/Cu_6Sn_5 MPs with feature sizes of 3-8 μm are composed of numerous uniform nanoparticles (100-200 nm) and plenty of voids. Compared with similar Sn-based electrodes in this work and other published reports, the as-prepared electrode delivers more outstanding electrochemical performance with a superior reversible capacity of 1.90 mAh cm^{-2}, 84.44% capacity retention and >99.5% coulombic efficiency upon 200 cycles. The cycling stability and integrity of the overall structure of the composite electrode have been greatly enhanced under the synergistic effect of buffer effect of copper as the inactive component, the unique hierarchical porous electrode architecture and the effective limitation in three dimensions of 3D-PCF skeleton. We are confident that this work can provide new-generation LIBs with a promising anode candidate and the facile method of dealloying and subsequent filling step can achieve the practical production and application of high-performance LIBs.

***Keywords*:** Lithium ion battery; Sn-Cu alloy; Hierarchical porous structure; Dealloying; Anode

Ⅰ. INTRODUCTION

LITHIUM-ION batteries (LIBs) are widely used as energy sources in varieties of portable devices on account of the high energy density, long cycle life and almost no pollution.[1, 2, 3] With rapid development of these devices and the promotion of new energy vehicles, the power density and energy density of LIBs are put forward higher requirements.[4-6] Nevertheless, the low theoretical specific capacity (372 mAh g^{-1}, LiC_6) and lithiation potential (close to the deposition potential of metal lithium) of graphite material limit the more extensive applications of LIBs.[7, 8] Therefore, to meet the growing demands, the advanced anode materials with high capacity and security are in urgent need of development. In recent years, a mass of novel materials has been developed by investigators as anodes for enhanced LIBs.[9-15] The metallic Sn is regarded as the most desirable candidate among these materials by reason of the high theoretical specific capacity (994 mAh g^{-1}, $Li_{22}Sn_5$), excellent electronic conductivity, safe lithiation potential and environmental friendliness.[16-18]

Unfortunately, tremendous volume change occurs during the Li-Sn alloying/de-alloying processes inevitably, which leads to severe pulverization, shedding and consequent loss of electrical connection between active substance and the current collector.[19-21] The damage to electrode will lead to sharp decline in capacity and poor cycling performance, which remain as a critical difficulty for further improvement and application of Sn-based electrodes. Recently, several potential approaches have been put forward to overcome the restrictions possessed by Sn active material. One promising approach is to build active/inactive composite

(such as Sn-Fe,[22-24] Sn-Ni,[25-27] Sn-Co,[28-30] and Sn-Cu[31-33]) by introducing inactive components, in which the inert and nonreactive material can buffer the volume expansion effectively during the lithiation/de-lithiation processes. For example, Leigang Xue, et al. developed the Sn-Cu alloy anode with improved cycling stability over 100 cycles for LIBs by electroless-plating of Sn on copper foam.[34] Another approach is refining electrode materials to nanoscale dimensions, such as nanoparticles, nanowires, nanorods and nanoporous structures, which can limit the volume expansion to nanoscale dimensions effectively.[35-37] The Gregorio F. Ortiz group reported the electrodeposition of Cu-Sn nanowires on Ti foils for rechargeable LIBs, delivering 295 mAh g^{-1} capacity upon 100 cycles stably.[38] John B. Cook, et al. reported nanoporous Sn with a granular hierarchical ligament morphology as anode for LIBs with more than 72% capacity retention and 693 mAh g^{-1} capacity over 350 cycles.[39] Additionally, due to the restriction in three dimensions and a larger specific surface area for loading more active materials, the three-dimensional porous current collector is more advantageous structurally in restricting volume strain and enhancing electrochemical reactions compared with two-dimensional planar current collector.

Herein, three-dimensional nanoporous Cu/Cu_6Sn_5 microparticles (3D-NP Cu/Cu_6Sn_5 MPs) were prepared by one-step chemical dealloying of $Cu_{20}Sn_{80}$ (at. %) alloy slices in the mixed aqueous solution of HF and HNO_3, and filled into the three-dimensional porous copper foam (3D-PCF) skeleton subsequently as 3D-PCF@Cu/Cu_6Sn_5 anode for LIBs. Compared with the electrodes prepared by electroless deposition of Cu_6Sn_5 on 3D-PCF (3D-PCF@Cu_6Sn_5) and coating the

planar copper foil with the microparticles (2D-CF@Cu/Cu_6Sn_5), the as-prepared 3D-PCF@Cu/Cu_6Sn_5 electrode delivered a superior reversible areal specific capacity of 1.90 mAh cm^{-2} and the more outstanding cycling performance of 84.44% capacity retention and >99.5% coulombic efficiency upon 200 cycles owing to its unique hierarchical porous structure, buffering effect of active/inactive system and limitation in three dimensions of 3D-PCF skeleton. Significantly, the method of one-step chemical dealloying and subsequent filling step like coating, which combines the laboratory research of electrode materials with practical applications, is suitable for large-scalable industrial production and commercialization of high-capacity electrodes for LIBs. We are confident that this work can provide a promising anode candidate and a facile preparation method with the universal applicability to other high-capacity electrode materials for the practical application of new-generation LIBs.

Ⅱ. EXPERIMENTAL

The Cu-Sn precursor alloy with a nominal composition of $Cu_{20}Sn_{80}$ (at. %) was prepared by melting pure Cu (99.99 wt. %) and pure Sn (99.99 wt. %) in a vacuum induction furnace under the protective atmosphere of argon. To ensure the uniformity of the chemical composition, the ingot has been remelted for three times. After removing the oxides on the surface, the alloy ingot was cut into 500 μm slices by wire-cutting EDM, and the greasy dirt occurred in wire-cutting was removed by ultrasonic cleaning in acetone solution. Ultimately, grind off the oxide skin with silicon carbide sandpaper and polish the alloy slices.

The polished slices were subjected to one-step dealloying in mixed aqueous

111 solution of 2 wt. % HF and 1 wt. % HNO_3 at 25 ℃ for three days in a water bath. The
112 as-dealloyed particle samples were washed for several times in deionized water and
113 alcohol solution to wash off the residual chemical reagents and dried in a vacuum
114 oven at 75 ℃ for 12h.

115 The active 3D-NP Cu/Cu_6Sn_5 MPs, conductive carbon black, and polyvinylidene
116 fluoride were mixed thoroughly in a weight ratio of 8:1:1 and dispersed in
117 N-methyl-2-pyrrolidinone solvent. To prepare 3D-PCF@Cu/Cu_6Sn_5 electrode, the
118 electrode slurry was filled into 3D-PCF as working electrode, which was dried at 75
119 ℃ in vacuum for 12h. As a contrast, the slurry is poured carefully and spread evenly
120 and smoothly on the clean copper foil surface to form the final 2D-CF@Cu/Cu_6Sn_5
121 electrode, which is dried at 75 ℃ in vacuum for 12h. Simultaneously,
122 3D-PCF@Cu_6Sn_5 electrode was prepared by electroless deposition of Cu_6Sn_5 on
123 3D-PCF in a plating bath mainly including 1 M thiourea, 0.1 M $SnSO_4$, 0.85 M
124 concentrated H_2SO_4 and 0.5 M sodium hypophosphite at 25 ℃ for 3min. The loading
125 mass of active 3D-NP Cu/Cu_6Sn_5 MPs for 3D-PCF@Cu/Cu_6Sn_5 and
126 2D-CF@Cu/Cu_6Sn_5 electrodes is about 20-25 mg cm^{-2} (4.3-5.4 mg cm^{-2} for tin), and
127 the 3D-PCF@Cu_6Sn_5 electrode shows close loading mass of tin (about 5 mg cm^{-2}).
128 All of the electrodes were pressed at 25 MPa for 2 minutes using BJ-30 tablet press to
129 flatten the electrode for easy battery assembly. All of the chemical reagents used in
130 the work are analytical grade and do not need to be purified again.

131 X-ray powder diffraction (XRD, Rigaku D/Max-2400) was used for investigation
132 of phase composition with Cu K_α radiation from 20° to 80°. Microstructural

characterization and chemical composition analysis of the samples were performed using field-emission scanning electron microscopy (FESEM, Hitachi S-4800) with an energy dispersive X-ray (EDX) spectroscopy analyzer and transmission electron microscopy (TEM, JEOL JEM 2100F). Nitrogen adsorption/desorption measurements were performed with Kubo X1000 analyzer.

CR2032 coin-type cells were assembled in an argon-filled glove box (LS-750D, DELLIX) with the concentrations of moisture and oxygen below 0.1 ppm by using 1 M $LiPF_6$ dissolved in ethylene carbonate/dimethyl carbonate (1:1 v/v) as electrolyte. Pure lithium foil was used as counter and reference electrode and poly-propylene film (Celgard 2400) was used as separator. Prior to the electrochemical tests, each half-cell was aged for 24h at room temperature. A multichannel battery measurement system (NEWARE BTS-610, Neware Technology Co., Ltd., China) was used for the galvanostatic charge/discharge and rate tests in the potential range of 0.01-1.5 V (vs. Li/Li^+) at room temperature. A CHI760E electrochemical workstation was used for cyclic voltammograms (CVs) tests in a potential range of 0.01 and 1.5 V (vs. Li/Li^+) at a scan rate of 0.1 mV s^{-1} and electrochemical impedance spectroscopy (EIS) tests over a frequency range from 0.01 Hz to 1 MHz with AC amplitude of 5 mV.

Ⅲ. RESULTS AND DISCUSSION

The EDX result of the original $Cu_{20}Sn_{80}$ (at. %) precursor alloy is shown in Fig. S1 (see electronic supplementary data file). The atomic percentages of Cu and Sn are 20.39 and 79.61 respectively, which are consistent well with the designed chemical components of the $Cu_{20}Sn_{80}$ alloy and prove that the alloy can be used in subsequent

dealloying process. Fig. 1 shows the schematic diagram of preparation process of 3D-NP Cu/Cu_6Sn_5 MPs and 3D-PCF@Cu/Cu_6Sn_5 electrode. The $Cu_{20}Sn_{80}$ alloy slice was dealloyed firstly in the mixed aqueous solution of 2 wt. % HF and 1 wt. % HNO_3, and the as-obtained 3D-NP Cu/Cu_6Sn_5 MPs were mixed with conductive agent and binder and filled into the 3D-PCF skeleton together as anode subsequently.

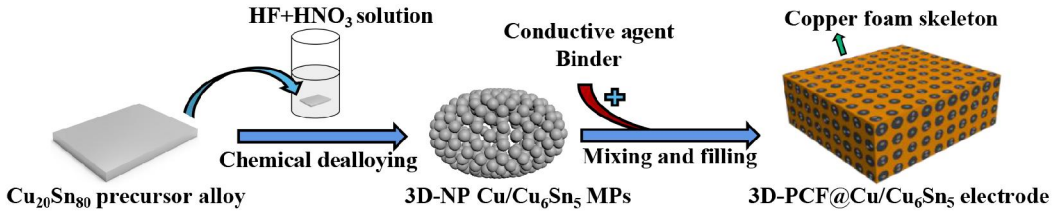

Figure 1—Schematic diagram of preparation process of 3D-NP Cu/Cu_6Sn_5 MPs and 3D-PCF@Cu/Cu_6Sn_5 electrode.

Fig. 2a and 2b show the microstructure of 3D-NP Cu/Cu_6Sn_5 MPs. Fig. 2a demonstrates the irregular ellipsoidal morphology of microparticles with the feature sizes of 3-8 μm. As the main body of the precursor alloy, tin is corroded seriously first due to its high electrochemical activity, which leads to the collapse of the whole structure and the formation of composite particles with certain structure. As illustrated in Fig. 2b, it can be clearly seen that a single microparticle is composed of a mass of nanoparticles with the feature sizes of 100-200 nm and plenty of voids. The uniform nanoparticles and porous structure will be beneficial to the electrochemical performance extraordinarily. A great deal of nanoparticles with large specific surface area can provide sufficient active sites for the electrochemical reaction process, which greatly improves the utilization of active substances and leads to a higher capacity. Simultaneously, the porous channel structure is conducive to mass transfer process of

the electrochemical reaction and buffering the immense volume change, leading to the excellent rate and cycle performance. The EDX results in Fig. 2c show the element components of the microparticles after dealloying, with only 12.84 at. % of the tin element left. To confirm the phase compositions and crystal structures, Fig. 2d shows corresponding XRD patterns of $Cu_{20}Sn_{80}$ precursor alloy and microparticles after dealloying for 3d at 25 ℃. The red solid line in Fig. 2d is XRD pattern of precursor

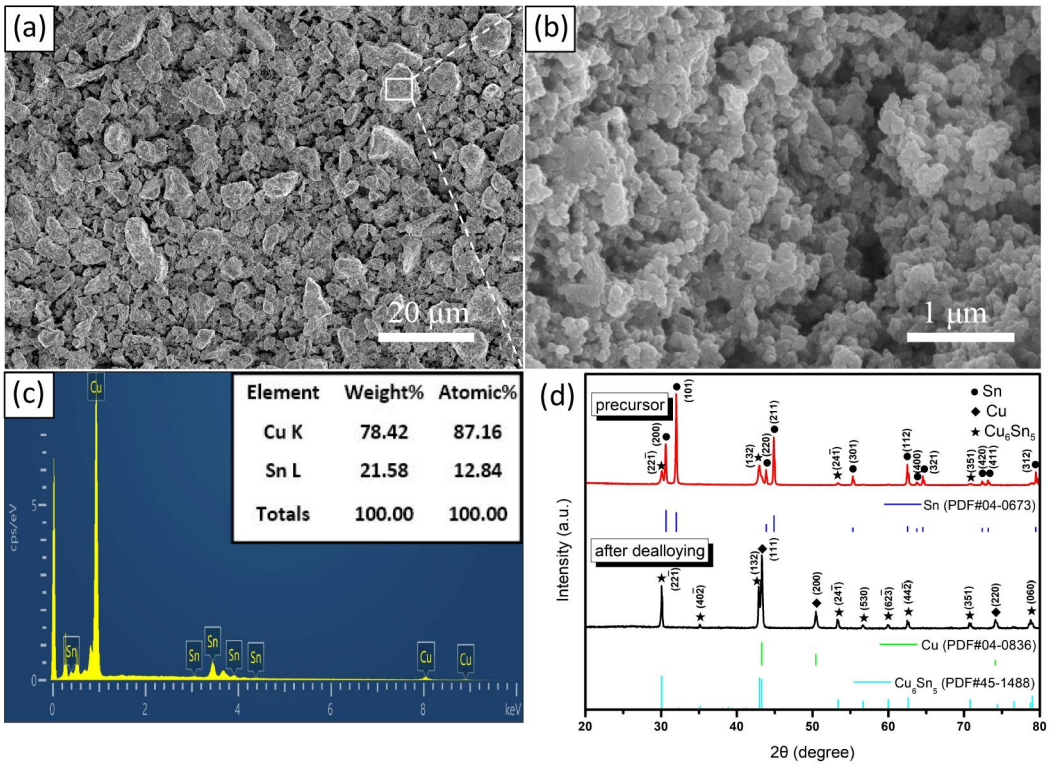

Figure 2—(a) SEM image, (b) high-magnification SEM image marked in part (a) and (c) the EDX results of 3D-NP Cu/Cu_6Sn_5 MPs. (d) XRD patterns of precursor $Cu_{20}Sn_{80}$ alloy (solid red line) and 3D-NP Cu/Cu_6Sn_5 MPs (solid black line) after dealloying for 3d at 25 ℃ in mixed aqueous solution of 2 wt. % HF and 1 wt. % HNO_3.

alloy. All the diffraction peaks can be indexed to tetragonal structure of Sn (PDF No. 04-0673) and monoclinic Cu_6Sn_5 (PDF No. 45-1488), which are consistent with the phase compositions of $Cu_{20}Sn_{80}$ alloy according to the binary phase diagram of Cu-Sn (Fig. S2). The black solid line in Fig. 2d shows the XRD pattern of the microparticles

after dealloying. All the diffraction peaks can be indexed to cubic copper (PDF No. 04-0836) and monoclinic Cu_6Sn_5 (PDF No. 45-1488). There is no corresponding diffraction peak of Sn in XRD pattern after dealloying, which proves that Sn phase is corroded completely first due to its relatively high electrochemical activity in mixed solution. The cubic copper came from the remaining Cu_6Sn_5 phase during subsequent dealloying process, in which the Sn was corroded away based on its relatively high electrochemical activity compared with copper element and the Cu was generated. Therefore, the phase compositions of microparticle can be proved to be Cu_6Sn_5 and Cu. The Cu metal in electrode materials has the following three functions: (1) as the main body of micron particles, the Cu metal plays an important role in supporting the whole structure; (2) the excellent electronic conductivity of Cu greatly promotes the transmission of electrons; (3) the chemically inert Cu metal is also in favor of buffering severe volume expansion and enhancing the cycling performance of batteries, which plays the same role as the element Cu in Cu_6Sn_5.

Typical TEM observation to reveal the porous structure of 3D-NP Cu/Cu_6Sn_5 MPs was carried out and shown in Fig. 3a. Apparently, the dark ligaments of nanoparticles and the inner bright pores form the porous structure jointly. Notably, a single 100-200 nanoparticle (dark region) is also composed of plenty of smaller nanoparticles and nanopores. Furthermore, the HRTEM (Fig. 3b) image proves the lattice fringes of nanoparticles. The distinct lattice spacing of 0.323, 0.297 and 0.210 nm corresponds to $(31\bar{1})$, $(22\bar{1})$, and (132) planes of Cu_6Sn_5 phase, while the lattice spacing of 0.209 and 0.181 nm corresponds to (111) and (200) of Cu phase, further confirming that the

composite particle is composed of Cu_6Sn_5 and Cu phase.

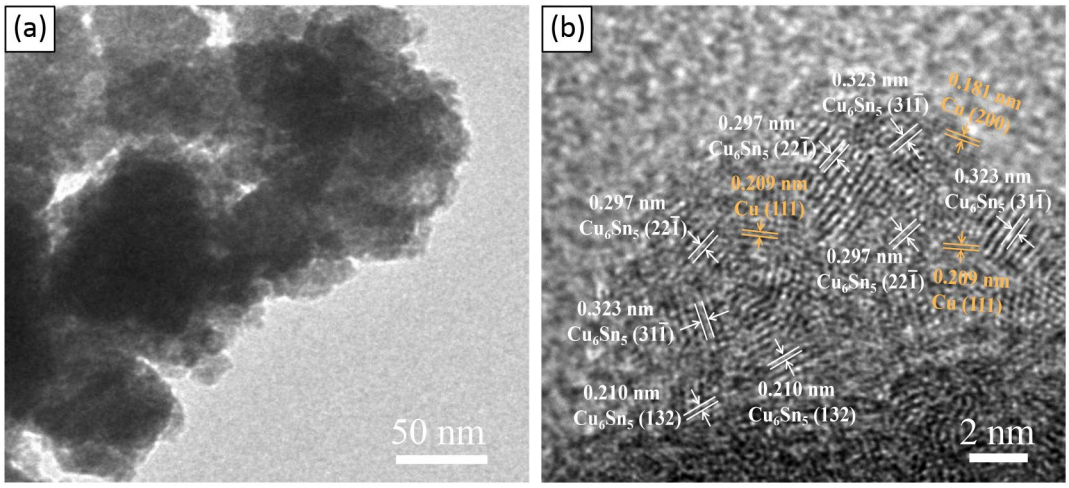

Figure 3—(a) TEM and (b) HRTEM images of 3D-NP Cu/Cu_6Sn_5 MPs.

The nanoporous feature of the 3D-NP Cu/Cu_6Sn_5 MPs was demonstrated by nitrogen adsorption/desorption tests (Fig. S3). The N_2 adsorption/desorption isotherms display the type IV isotherms with a representative H_3-type hysteresis loop, indicating the meso-porosity. The pore size distribution (inset of Fig. S3) according to the Barrett-Joyner-Halenda (BJH) method, indicates a narrow pore size distribution in the range of 3-5 nm and a broad distribution (dozens of nanometers) of these 3D-NP Cu/Cu_6Sn_5 MPs. Meanwhile, the specific surface area calculated from Brunauer-Emmett-Teller (BET) method is as large as 6.1 $m^2\ g^{-1}$.

The electrochemical performance of as-prepared 3D-PCF@Cu/Cu_6Sn_5 electrode is evaluated by coin-type cell, in which the metal Li foil was used as counter and reference electrodes. The diffraction peaks of 3D-PCF@Cu/Cu_6Sn_5 electrode can be indexed to cubic copper and monoclinic Cu_6Sn_5 (see the XRD patterns in Fig. S4),

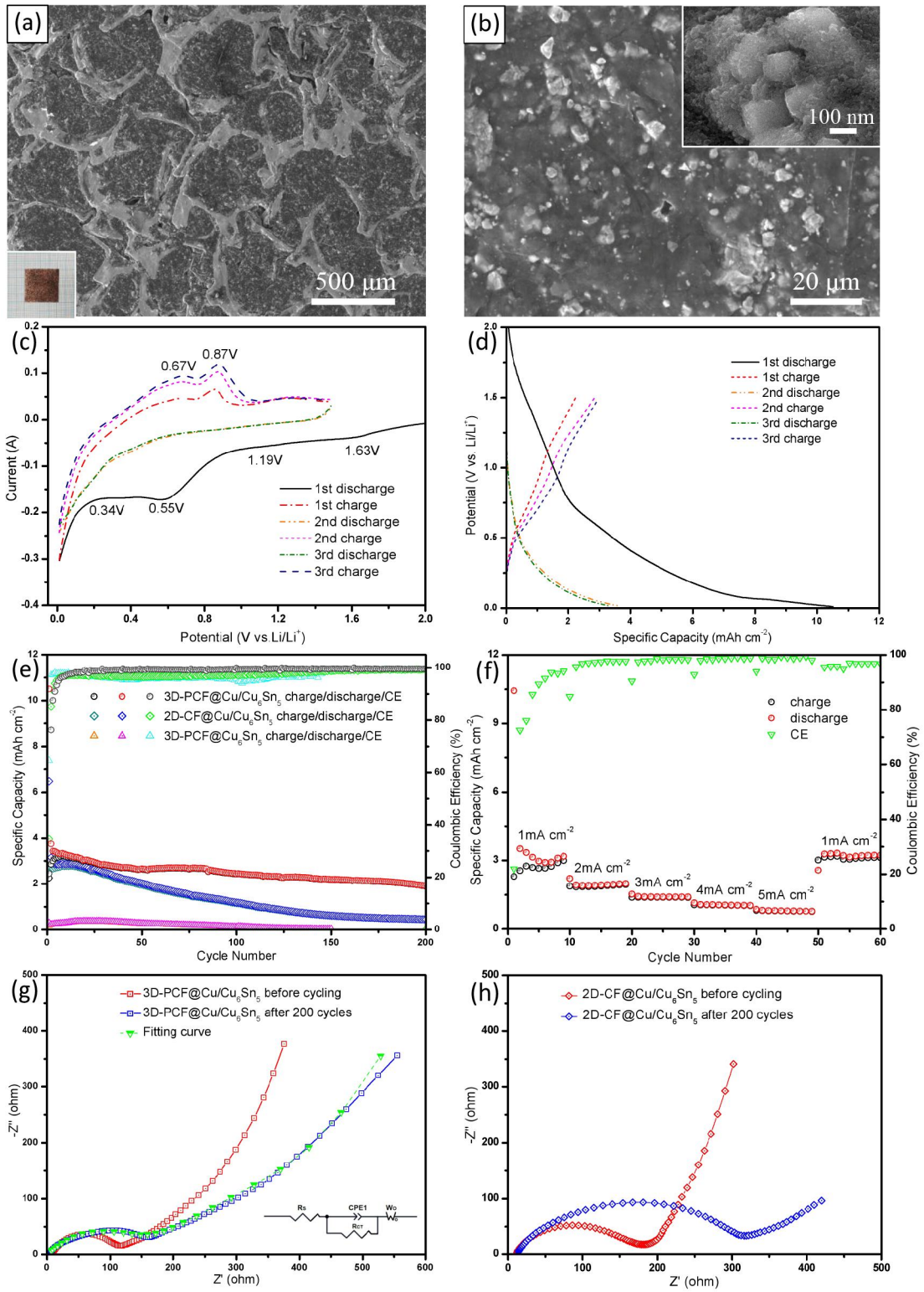

Figure 4—(a, b) SEM images of electrode morphology of 3D-PCF@Cu/Cu_6Sn_5. The inset in part (a) is the corresponding macrograph of electrode and the inset in part (b) is high-magnification SEM image of 3D-NP Cu/Cu_6Sn_5 MPs in as-prepared electrode. (c) CVs of 3D-PCF@Cu/Cu_6Sn_5 electrode for the first three cycles ranging from 0.01 to 1.5 V (vs. Li/Li^+) at scan rate of 0.1 mV s^{-1}. (d) Galvanostatic charge-discharge profiles of 3D-PCF@Cu/Cu_6Sn_5 electrode at a current density of 1 mA cm^{-2}. (e)

Cycling performance of 3D-PCF@Cu/Cu_6Sn_5, 2D-CF@Cu/Cu_6Sn_5 and 3D-PCF@Cu_6Sn_5 electrodes at a current density of 1 mA cm^{-2}. (f) Rate capability of 3D-PCF@Cu/Cu_6Sn_5 electrode at current density up to 5 mA cm^{-2}. (g, h) Nyquist plots of 3D-PCF@Cu/Cu_6Sn_5 and 2D-CF@Cu/Cu_6Sn_5 electrodes before and after 200 cycles. The inset in part (g) is the relevant fitting circuit of 3D-PCF@Cu/Cu_6Sn_5 electrode after 200 cycles.

where the Cu_6Sn_5 exhibits relatively weak intensity of diffraction peaks due to the presence of 3D-PCF skeleton and the wide peak below 35° belongs to carbon. Fig. 4a shows the SEM image of electrode morphology of 3D-PCF@Cu/Cu_6Sn_5 and the inset in the bottom left corner is the macrograph of corresponding electrode. It is clear that the pressed 3D-PCF skeleton is densely filled with electrode slurry of 3D-NP Cu/Cu_6Sn_5 MPs, conductive agent and binder. The micron 3D-PCF skeleton, micron composite particles and nanoporous structure of Cu/Cu_6Sn_5 constitute the unique hierarchical porous structure jointly and enhance the electrochemical performance of the electrode. The 3D-PCF skeleton can buffer and restrict the mechanical strain occurring in the charge/discharge processes, which effectively prevents the destruction and shedding of active materials. Meanwhile, the close contact between 3D-PCF skeleton and the slurry constitutes a desirable conductive network which is beneficial to electrochemical reactions. Additionally, the SEM image of slurry in 3D-PCF skeleton is displayed in Fig. 4b, in which, the microparticles are evenly embedded and dispersed, proving the excellent quality of prepared slurry without agglomeration phenomena on a large scale. As shown in the inset in Fig. 4b, the single micron particle remains its original structure in the prepared electrode and is uniformly covered by fine binder and conductive agent. The typical SEM images of

electrode morphology of 2D-CF@Cu/Cu_6Sn_5 and 3D-PCF@Cu_6Sn_5 are also shown in Fig. S5 and S6.

Fig. 4c presents the cyclic voltammograms of the first three cycles of 3D-PCF@Cu/Cu_6Sn_5 electrode at the scan rate of 0.1 mV s^{-1} with the voltage range from 0.01 to 1.5 V (vs. Li /Li^+). The reduction peaks at 1.63 V and 1.19 V during the first cathodic scan can be put down to the reduction of some oxides and the formation of solid electrolyte interface (SEI) layer on the surface of the electrode, respectively.[40] A reduction peak appears at 0.55 V, which is assigned to the intercalation process of Li into Cu_6Sn_5 to form Li_2CuSn and Cu described by Equation (1),[41, 42] and disappears in subsequent cycles, indicating that the intercalation process only happens in first cycle. After that, a gentle peak at 0.34 V and a distinct peak below 0.2 V are observed, involving step-by-step lithiation processes to finally form $Li_{4.4}Sn$ described by Equation (2).[41, 43-45] It is worth noting that, the disappeared cathodic peaks larger than 1 V from the second cycle prove that the SEI layer and partial irreversible reactions mainly occur in the first cycle. In the anodic sweep processes, the distinct oxidation peaks appear at 0.87 V and 0.67 V, which are attributed to multistep de-lithiation of $Li_{4.4}Sn$ described by Equation (3).[40, 43] After the first cycle, active tin participates in subsequent cycles described by Equation (3) and Equation (4) and the excellent electrochemical reversibility is demonstrated by the good coincidence of the curves.

$$Cu_6Sn_5+10Li^++10e^-\rightarrow 5Li_2CuSn+Cu \text{ (1st discharge)} \quad (1)$$

$$5Li_2CuSn+12Li^++12e^-\rightarrow 5Li_{4.4}Sn+5Cu \text{ (1st discharge)} \quad (2)$$

285 $Li_{4.4}Sn \rightarrow Sn+4.4Li^{+}+4.4e^{-}$ (1st charge and subsequent charge) (3)

286 $Sn+4.4Li^{+}+4.4e^{-} \rightarrow Li_{4.4}Sn$ (discharge after 1st cycle) (4)

287 Fig. 4d shows the typical galvanostatic charge-discharge profiles of
288 3D-PCF@Cu/Cu_6Sn_5 electrode at a current density of 1 mA cm^{-2} and in a potential
289 range of 0.01 and 1.5 V (vs. Li/Li^{+}). The discharge and charge specific capacities of
290 1^{st}, 2^{nd} and 3^{rd} cycles are 10.51, 3.74, 3.42 mAh cm^{-2} and 2.25, 2.85, 2.99 mAh cm^{-2},
291 respectively. The low coulombic efficiency of first cycle is 21.41% only and increases
292 to 76.2% and 87.4% immediately in the next two cycles. It is in connection with the
293 formation of massive SEI layer on electrode with large specific surface area and
294 irreversible side reactions, which consume a mass of Li^{+} inevitably in the first
295 discharge process. The charge specific capacity increases in first several cycles,
296 mainly owing to the activation of electrode and utilization of the active materials
297 gradually. This phenomenon is consistent with the increasing tendency of the CVs
298 area which represents the capacity during the charge processes in Fig. 4c.

299 The 3D-PCF@Cu/Cu_6Sn_5 electrode demonstrates the more impressive
300 electrochemical performance than 2D-CF@Cu/Cu_6Sn_5 and 3D-PCF@Cu_6Sn_5
301 electrodes between 0.01 and 1.5 V at a current density of 1 mA cm^{-2} (Fig. 4e). The
302 initial charge specific capacity of 3D-PCF@Cu/Cu_6Sn_5 electrode is shown as 2.25
303 mAh cm^{-2}. As a comparison, the 2D-CF@Cu/Cu_6Sn_5 electrode shows a similar initial
304 charge capacity of 2.24 mAh cm^{-2} at the same current density, with the initial
305 discharge capacity and coulombic efficiency of 6.48 mAh cm^{-2} and 34.57%
306 respectively. After several cycles, the coulombic efficiency of 3D-PCF@Cu/Cu_6Sn_5

electrode increased rapidly to more than 98% and close to 100% during subsequent cycles, which indicates the excellent reversibility and is higher than that of 2D-CF@Cu/Cu_6Sn_5 electrode. Simultaneously, the 3D-PCF@Cu/Cu_6Sn_5 electrode shows a better cyclic stability. After 200 cycles, the high reversible capacity of 1.90 mAh cm^{-2} and capacity retention of 84.44% with the >99.5% coulombic efficiency compared with the first charge capacity are shown, which are much higher than 0.48 mAh cm^{-2} reversible capacity and 21.43% capacity retention of 2D-CF@Cu/Cu_6Sn_5 electrode. This is mainly due to the fact that the 3D-PCF skeleton can effectively limit the volume expansion to its interior, buffer volumetric stress and avoid the pulverization and shedding of active particles, resulting in a great improvement in the cycling and structural stabilities of electrode. Additionally, at close loading mass of tin and phase composition (see the XRD patterns in Fig. S7), 3D-PCF@Cu/Cu_6Sn_5 electrode shows a superior reversible specific capacity compared to 3D-PCF@Cu_6Sn_5 electrode with the highest capacity of 0.37 mAh cm^{-2} only. This result indicates the extremely high utilization rate of active substances of 3D-PCF@Cu/Cu_6Sn_5 electrode, in which the large specific surface area and high-concentration active sites of 3D-NP Cu/Cu_6Sn_5 MPs effectively enhance the process of electrochemical reactions. On the contrary, the 2D planar distribution morphology of the active material for the 3D-PCF@Cu_6Sn_5 electrode leads to the small specific surface area and low concentration of active sites. Eventually, extremely low utilization of active materials and corresponding low capacity are obtained. Table S1 lists several similar Sn-based electrodes published in previous literature. It is clear that the area specific capacity

and cycle performance of 3D-PCF@Cu/Cu_6Sn_5 electrode are comparable with others.

For the sake of further studying its electrochemical performance, the rate performance of 3D-PCF@Cu/Cu_6Sn_5 electrode was performed and the result was shown in Fig. 4f, with the current densities from 1 mA cm^{-2} to 5 mA cm^{-2}. The specific capacities of 3D-PCF@Cu/Cu_6Sn_5 electrode vary from 2.99, 1.95, 1.38, 1.02 and 0.76 mAh cm^{-2} at the current density of 1, 2, 3, 4 and 5 mA cm^{-2}, respectively. After cycling at higher current densities, the ultra-high reversible capacity of 3.01 mAh cm^{-2} can be immediately recovered when the current density came back to 1 mA cm^{-2}, which is the same as that of 10^{th} cycle and verifies the excellent rate capability and electrochemical reversibility. The 3D-PCF skeleton for maintaining the stability of electrode integrally, highly conductive network for convenient electronic transmission and unique hierarchical porous structure for rapid mass transfer process in electrochemical reactions bring about the prominent rate performance together.

The merits of the 3D-PCF@Cu/Cu_6Sn_5 electrode were further confirmed by electrochemical impedance spectroscopy analysis in the frequency range from 0.01 Hz to 1 MHz with an amplitude of 5 mV.[46] Fig. 4g, 4h and S8 show the Nyquist plots of 3D-PCF@Cu/Cu_6Sn_5, 2D-CF@Cu/Cu_6Sn_5 and 3D-PCF@Cu_6Sn_5 electrodes before and after cycles, respectively. It is clear that all of the Nyquist plots are made up of a semicircle in high and medium frequency region, which is a corking indicator of the charge-transfer resistance (R_{ct}) and a sloping line in low frequency region associated with the diffusion of Li^+ through electrodes.[47-51] Obviously, the diameter of the semicircle related to 3D-PCF@Cu/Cu_6Sn_5 which represents the R_{ct}, is about 120 Ω

only before cycling, while the R_{ct} for 2D-CF@Cu/Cu_6Sn_5 electrode is about 190 Ω. The minor R_{ct} of 3D-PCF@Cu/Cu_6Sn_5 electrode verifies that the overall highly conductive 3D-PCF network effectively accelerates the kinetic processes for charge-transfer. Simultaneously, the equivalent circuit of 3D-PCF@Cu/Cu_6Sn_5 electrode after cycles used for fitting is shown in the inset of Fig. 4g, which consists of corresponding circuit models including the electrolyte resistance (R_s), charge transfer resistance (R_{ct}), Warburg impedance of Li^+ diffusion in electrode (W_o) and space charge capacitance at electrode/electrolyte interface (CPE1). The present fitting result exhibits that the resistance of 3D-PCF@Cu/Cu_6Sn_5 electrode increases slightly to 134.7 Ω after 200 cycles, proving the stability of electrode structure attributing to the restriction of 3D-PCF skeleton in three dimensions and buffer effect of hierarchical porous structure. However, a notable increase of resistance occurs in 2D-CF@Cu/Cu_6Sn_5 electrode and about 340 Ω of resistance can be obtained after 200 cycles, indicating the charge-transfer process is greatly hindered, which exists in 3D-PCF@Cu_6Sn_5 electrode (R_{ct} is about 400 Ω after 150 cycles) analogously. The reason for this phenomenon will be revealed further.

Fig. 5 shows the SEM images of 3D-PCF@Cu/Cu_6Sn_5 and 2D-CF@Cu/Cu_6Sn_5 electrodes after 200 cycles. It can be clear seen that the morphology of 3D-PCF@Cu/Cu_6Sn_5 electrode after cycles has no great change compared with that before cycling, where the electrode slurry is well filled in the 3D-PCF skeleton and no obvious destruction and shedding of active materials can be found. Nevertheless, the cracks, shedding and partial exfoliation of electrode materials from current collector

happened in 2D-CF@Cu/Cu_6Sn_5 electrode massively, which was the mainly reason for decay of capacity and increase of impedance. Meanwhile, the SEM images of 3D-PCF@Cu_6Sn_5 electrode after 150 cycles are displayed in Fig. S9. Compared with the morphology before cycling, the overall skeleton of the electrode did not change significantly, but obvious cracks and damage appeared on the electrode due to serious volume expansion during cycling. These results above demonstrate that the 3D-PCF@Cu/Cu_6Sn_5 electrode represents excellent transfer characteristics of lithium ions and electrons and structural stability under the synergistic effect of the nanoporous structure of Cu/Cu_6Sn_5 MPs and restriction in three dimensions of 3D-PCF skeleton.

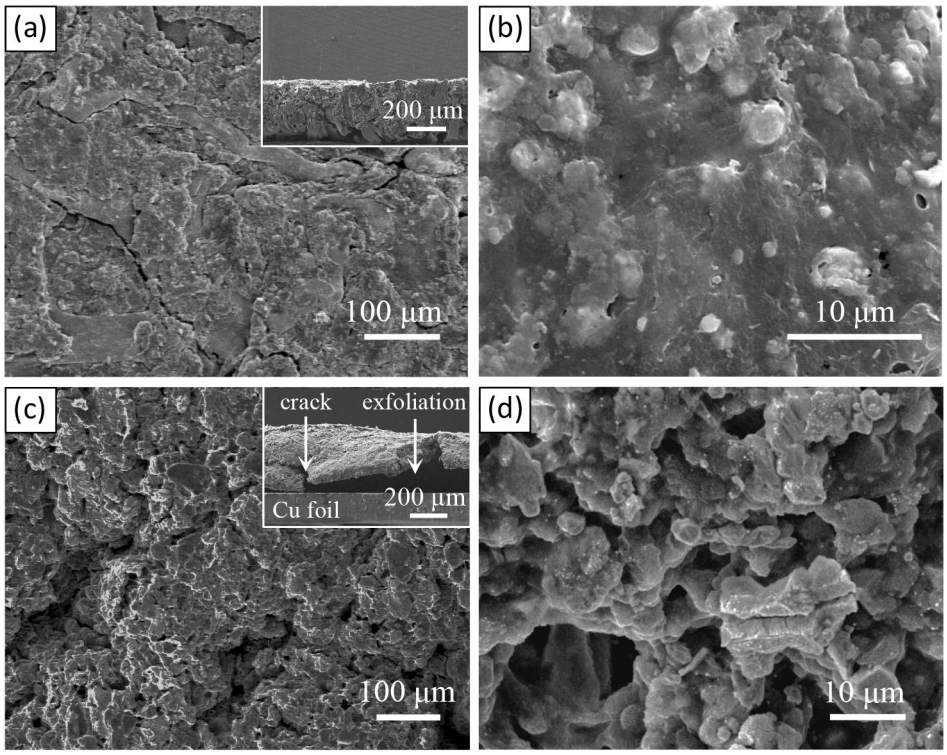

Figure 5—SEM images of (a, b) 3D-PCF@Cu/Cu_6Sn_5 and (c, d) 2D-CF@Cu/Cu_6Sn_5 electrodes after 200 cycles. The insets in part (a) and (c) are SEM images of cross sections of the corresponding electrodes.

Ⅳ. CONCLUSIONS

To summarize, we fabricated three-dimensional nanoporous Cu/Cu_6Sn_5 microparticles by one-step chemical dealloying of $Cu_{20}Sn_{80}$ alloy slices in the mixed solution of HF and HNO_3, and filled the microparticles into 3D-PCF skeleton subsequently as anode for LIBs. The microparticles with feature sizes of 3-8 μm are composed of uniform porous 100-200 nm Cu/Cu_6Sn_5 nanoparticles and a large amount of void space, and limited to 3D-PCF skeleton as active materials. Compared with 3D-PCF@Cu_6Sn_5 and 2D-CF@Cu/Cu_6Sn_5 electrodes, the 3D-PCF@Cu/Cu_6Sn_5 electrode exhibits higher reversible capacity of 1.90 mAh cm^{-2} and excellent cycling stability with the 84.44% capacity retention and >99.5% coulombic efficiency upon 200 cycles, respectively. The cycling stability and integrity of the overall structure of the composite electrode have been greatly enhanced under the synergistic effect of the buffer effect of copper as an inactive component, the hierarchical porous structure and the effective limitation in three dimensions of 3D-PCF skeleton. We are confident that the high specific capacity, long cycle life, stable electrode structure, facile preparation method and low cost of the 3D-PCF@Cu/Cu_6Sn_5 electrode will be the promising anode candidate towards new-generation LIBs, and the facile method of electrode preparation is expected to achieve practical production and has the universal applicability to other high-capacity electrode materials.

ACKNOWLEDGMENTS

We give thanks to financial support by the National Natural Science Foundation of China (51604177), the State Key Basic Research Program of PRC (2013CB934001),

the Research Grants Council of the Hong Kong Special Administrative Region, China (GRF PolyU152174/17E), the Hong Kong Scholars Program (XJ2014045, G-YZ67), the China Postdoctoral Science Foundation (2015M570784), the International S&T Innovation Cooperation Program of Sichuan Province (2020YFH0039), the Chengdu International S&T Cooperation Funded Project (2019-GH02-00015-HZ), the "1000 Talents Plan" of Sichuan Province, the Fundamental Research Funds for the Central Universities, the Experimental Technology Project of Sichuan University (20200080), and the Talent Introduction Program of Sichuan University (YJ201410). Additionally, the authors specially thank Dr. Shanling Wang (Analytical & Testing Center, Sichuan University) for help in TEM characterization.

CONFLICT OF INTEREST

The authors declare no conflict of interest.

ELECTRONIC SUPPLEMENTARY MATERIAL

The online version of this article (https://) contains supplementary material, which is available to authorized users.

REFERENCES

1. J.M. Tarascon and M. Armand: *Nature*, 2001, vol. 414, pp. 359-367.

2. J.B. Goodenough and Y. Kim: *Chem. Mater.*, 2010, vol. 22, pp. 587-603.

3. H. Liu, X. Liu, S. Wang, H. Liu and L. Li: *Energy Storage Materials*, 2020, vol. 28, pp. 122-145.

4. Y. Idota, T. Kubota, A. Matsufuji, Y. Maekawa and T. Miyasaka: *Science*, 1997, vol. 276, pp. 1395-1397.

5. M.N. Obrovac, L. Christensen, D.B. Le and J.R. Dahn: *J. Electrochem. Soc.*, 2007, vol. 154, pp. A849.

6. B.M. Bang, J. Lee, H. Kim, J. Cho and S. Park: *Adv. Energy Mater.*, 2012, vol. 2, pp. 878-883.

7. D.S. Su and R. Schlogl: *ChemSusChem*, 2010, vol. 3, pp. 136-168.

8. S. Yang, S. Wang, X. Liu and L. Li: *Carbon*, 2019, vol. 147, pp. 540-549.

9. S. Yang, W. Yue, J. Zhu, Y. Ren and X. Yang: *Adv. Funct. Mater.*, 2013, vol. 23, pp. 3570-3576.

10. D. Deng, M.G. Kim, J.Y. Lee and J. Cho: *Energ. Environ. Sci.*, 2009, vol. 2, pp. 818.

11. J. Zhu, X. Zhang, C. Zeng, A. Liu and G. Hu: *Mater. Lett.*, 2017, vol. 209, pp. 338-341.

12. L. Xia, S. Wang, G. Liu, L. Ding, D. Li, H. Wang and S. Qiao: *Small*, 2016, vol. 12, pp. 853-859.

13. P. Lian, X. Zhu, S. Liang, Z. Li, W. Yang and H. Wang: *Electrochim. Acta*, 2011,

454 vol. 56, pp. 4532-4539.

455 14. S. Shi, T. Deng, M. Zhang and G. Yang: *Electrochim. Acta*, 2017, vol. 246, pp.

456 1104-1111.

457 15. Y. Cheng, Z. Yi, C. Wang, Y. Wu and L. Wang: *Chem. Eng. J.*, 2017, vol. 330, pp.

458 1035-1043.

459 16. X. Wu, Y. Guo and L. Wan: *Chemistry - An Asian Journal*, 2013, vol. 8, pp.

460 1948-1958.

461 17. Y. Idota, T. Kubota, A. Matsufuji, Y. Maekawa and T. Miyasaka: *Science*, 1997,

462 vol. 276, pp. 1395-1397.

463 18. S.Y. Hong, Y. Kim, Y. Park, A. Choi, N. Choi and K.T. Lee: *Energ. Environ. Sci.*,

464 2013, vol. 6, pp. 267-281.

465 19. M. Winter and J.O. Besenhard: *Electrochim. Acta*, 1999, vol. 45, pp. 31-50.

466 20. S. Yang, P.Y. Zavalij and M.S. Whittingham: *Electrochem. Commun.*, 2003, vol.

467 5, pp. 587-590.

468 21. S.D. Beattie and J.R. Dahn: *J. Electrochem. Soc.*, 2003, vol. 150, pp. A894.

469 22. H. Shi, Z. Fang, X. Zhang, F. Li, Y. Tang, Y. Zhou, P. Wu and G. Yu: *Nano Lett.*,

470 2018, vol. 18, pp. 3193-3198.

471 23. F. Xin, H. Zhou, Q. Yin, Y. Shi, F. Omenya, G. Zhou and M.S. Whittingham:

472 *ACS Omega*, 2019, vol. 4, pp. 4888-4895.

473 24. R. Zhang, S. Upreti and M. Stanley Whittingham: *J. Electrochem. Soc.*, 2011, vol.

474 158, pp. A1498.

475 25. X. Dong, W. Liu, X. Chen, J. Yan, N. Li, S. Shi, S. Zhang and X. Yang: *Chem.*

476 *Eng. J.*, 2018, vol. 350, pp. 791-798.

477 26. J. Liu, Y. Wen, P.A. van Aken, J. Maier and Y. Yu: *Nano Lett.*, 2014, vol. 14, pp.

478 6387-6392.

479 27. J. Hassoun, S. Panero and B. Scrosati: *J. Power Sources*, 2006, vol. 160, pp.

480 1336-1341.

481 28. J. Zhang and Y. Xia: *J. Electrochem. Soc.*, 2006, vol. 153, pp. A1466.

482 29. H. Guo, H. Zhao, X. Jia, X. Li and W. Qiu: *Electrochim. Acta*, 2007, vol. 52, pp.

483 4853-4857.

484 30. M. Valvo, U. Lafont, L. Simonin and E.M. Kelder: *J. Power Sources*, 2007, vol.

485 174, pp. 428-434.

486 31. X. Fan, Y. Shi, J. Wang, J. Wang, X. Shi, L. Xu, L. Gou and D. Li: *Solid State*

487 *Ionics*, 2013, vol. 237, pp. 1-7.

488 32. H.C. Shin and M. Liu: *Adv. Funct. Mater.*, 2005, vol. 15, pp. 582-586.

489 33. J. Chen, L. Yang, S. Fang and S. Hirano: *J. Power Sources*, 2012, vol. 209, pp.

490 204-208.

491 34. L. Xue, Z. Fu, Y. Yao, T. Huang and A. Yu: *Electrochim. Acta*, 2010, vol. 55, pp.

492 7310-7314.

493 35. Z. Wang, M. Wang, Z. Yang, Y. Bai, Y. Ma, G. Wang, Y. Huang and X. Li:

494 *ChemElectroChem*, 2017, vol. 4, pp. 345-352.

495 36. C. Wu, J. Maier and Y. Yu: *Adv. Funct. Mater.*, 2015, vol. 25, pp. 3488-3496.

496 37. B. Wang, B. Luo, X. Li and L. Zhi: *Mater. Today*, 2012, vol. 15, pp. 544-552.

497 38. G.F. Ortiz, M.C. López, R. Alcántara and J.L. Tirado: *J. Alloy. Compd.*, 2014, vol.

585, pp. 331-336.

39. J.B. Cook, E. Detsi, Y. Liu, Y. Liang, H. Kim, X. Petrissans, B. Dunn and S.H. Tolbert: *ACS Appl. Mater. Inter.*, 2016, vol. 9, pp. 293-303.

40. L. Sun, H. Cai, W. Zhang, X. Ren, P. Zhang and J. Liu: *Integr. Ferroelectr.*, 2016, vol. 171, pp. 193-202.

41. L. Su, J. Fu, P. Zhang, L. Wang, Y. Wang and M. Ren: *RSC Adv.*, 2017, vol. 7, pp. 28399-28406.

42. Y. Xing, S. Wang, B. Fang, Y. Feng and S. Zhang: *Micropor. Mesopor. Mat.*, 2018, vol. 261, pp. 237-243.

43. H.C. Shin and M. Liu: *Adv. Funct. Mater.*, 2005, vol. 15, pp. 582-586.

44. L. Xue, Z. Fu, Y. Yao, T. Huang and A. Yu: *Electrochim. Acta*, 2010, vol. 55, pp. 7310-7314.

45. J.S. Thorne, J.R. Dahn, M.N. Obrovac and R.A. Dunlap: *J. Power Sources*, 2012, vol. 216, pp. 139-144.

46. Y. Zhang, S. Yang, S. Wang, X. Liu, L. Li: *Energy Storage Materials*, 2019, vol. 18, pp. 447-455.

47. Y. Guo, X. Zeng, Y. Zhang, Z. Dai, H. Fan, Y. Huang, W. Zhang, H. Zhang, J. Lu, F. Huo and Q. Yan: *ACS Appl. Mater. Inter.*, 2017, vol. 9, pp. 17172-17177.

48. Q. Tang, Y. Cui, J. Wu, D. Qu, A.P. Baker, Y. Ma, X. Song and Y. Liu: *Nano Energy*, 2017, vol. 41, pp. 377-386.

49. S. Kang, X. Chen and J. Niu: *Nano Lett.*, 2017, vol. 18, pp. 467-474.

50. H. Wang, Q. Wu, D. Cao, X. Lu, J. Wang, M.K.H. Leung, S. Cheng, L. Lu and C.

Niu: *Materials Today Energy*, 2016, vol. 1-2, pp. 24-32.

51. X. Liang, J. Wang, S. Zhang, L. Wang, W. Wang, L. Li, H. Wang, D. Huang, W. Zhou and J. Guo: *Appl. Surf. Sci.*, 2019, vol. 476, pp. 28-35

Figure Captions

Figure 1—Schematic diagram of preparation process of 3D-NP Cu/Cu_6Sn_5 MPs and 3D-PCF@Cu/Cu_6Sn_5 electrode.

Figure 2—(a) SEM image, (b) high-magnification SEM image marked in part (a) and (c) the EDX results of 3D-NP Cu/Cu_6Sn_5 MPs. (d) XRD patterns of precursor $Cu_{20}Sn_{80}$ alloy (solid red line) and 3D-NP Cu/Cu_6Sn_5 MPs (solid black line) after dealloying for 3d at 25 ℃ in mixed aqueous solution of 2 wt. % HF and 1 wt. % HNO_3.

Figure 3—(a) TEM and (b) HRTEM images of 3D-NP Cu/Cu_6Sn_5 MPs.

Figure 4—(a, b) SEM images of electrode morphology of 3D-PCF@Cu/Cu_6Sn_5. The inset in part (a) is the corresponding macrograph of electrode and the inset in part (b) is high-magnification SEM image of 3D-NP Cu/Cu_6Sn_5 MPs in as-prepared electrode. (c) CVs of 3D-PCF@Cu/Cu_6Sn_5 electrode for the first three cycles ranging from 0.01 to 1.5 V (vs. Li/Li^+) at scan rate of 0.1 mV s^{-1}. (d) Galvanostatic charge-discharge profiles of 3D-PCF@Cu/Cu_6Sn_5 electrode at a current density of 1 mA cm^{-2}. (e) Cycling performance of 3D-PCF@Cu/Cu_6Sn_5, 2D-CF@Cu/Cu_6Sn_5 and 3D-PCF@Cu_6Sn_5 electrodes at a current density of 1 mA cm^{-2}. (f) Rate capability of 3D-PCF@Cu/Cu_6Sn_5 electrode at current density up to 5 mA cm^{-2}. (g, h) Nyquist plots of 3D-PCF@Cu/Cu_6Sn_5 and 2D-CF@Cu/Cu_6Sn_5 electrodes before and after 200 cycles. The inset in part (g) is the relevant fitting circuit of 3D-PCF@Cu/Cu_6Sn_5 electrode after 200 cycles.

Figure 5—SEM images of (a, b) 3D-PCF@Cu/Cu_6Sn_5 and (c, d) 2D-CF@Cu/Cu_6Sn_5

564 electrodes after 200 cycles. The insets in part (a) and (c) are SEM images of cross

565 sections of the corresponding electrodes.